Coherently coupled mechanical oscillators in the quantum regime

Pan-Yu Hou,[1,2,*] Jenny J. Wu,[1,2] Stephen D. Erickson,[1,2] Daniel C. Cole,[1] Giorgio Zarantonello,[1,2]
Adam D. Brandt,[1] Andrew C. Wilson,[1] Daniel H. Slichter,[1] and Dietrich Leibfried[1,†]
[1]*National Institute of Standards and Technology, 325 Broadway, Boulder, CO 80305, USA*
[2]*Department of Physics, University of Colorado, Boulder, CO 80309, USA*

(Dated: June 22, 2022)

arXiv:2205.14841v2 [quant-ph] 19 Jun 2022

Coupled harmonic oscillators are ubiquitous in physics and play a prominent role in quantum science. They are a cornerstone of quantum mechanics [1] and quantum field theory [2], where second quantization relies on harmonic oscillator operators to create and annihilate particles. Descriptions of quantum tunneling, beamsplitters, coupled potential wells, "hopping terms", decoherence, and many other phenomena rely on coupled harmonic oscillators. However, the ability to couple separate quantum harmonic oscillators directly, with coupling rates that substantially exceed decoherence rates, has remained elusive. Here, we realize high-fidelity coherent exchange of single motional quanta between harmonic oscillators – in this case, spectrally separated harmonic modes of motion of a trapped ion crystal – where the timing, strength, and phase of the coupling are controlled through an oscillating electric potential with suitable spatial variation. The coupling rate can be made much larger than the decoherence rates, enabling demonstrations of high-fidelity quantum state transfer, entanglement of motional modes, and Hong-Ou-Mandel-type interference [3]. We also project a harmonic oscillator into its ground state by measurement and preserve that state during repetitions of the projective measurement, an important prerequisite for non-destructive syndrome measurement in continuous-variable quantum error correction [4–6]. Controllable coupling between harmonic oscillators has potential applications in quantum information processing with continuous variables, quantum simulation, and precision measurements. It can also enable cooling and quantum logic spectroscopy [7] involving motional modes of trapped ions that are not directly accessible.

Quantum harmonic oscillators (HOs) are ubiquitous in models of nature and have a mathematically simple description based on creation and annihilation operators $\hat{a}^\dagger$ and $\hat{a}$, respectively [1]. For two different HO modes labeled as a and b, we designate the creation and annihilation operators $\{\hat{a}^\dagger, \hat{a}\}$ and $\{\hat{b}^\dagger, \hat{b}\}$ respectively. Combining the operators $\hat{a}^\dagger$ and $\hat{b}$ as $\hat{a}^\dagger\hat{b}$ models the creation of a quantized excitation in mode a while annihilating one excitation in mode b, as required for elementary descriptions of tunneling, beamsplitters, coupled potential wells, and "hopping terms" in solid state models. Incomplete exchange leads to entanglement between modes a and b, and models of decoherence can be realized by coupling a system a with a reservoir of unobserved oscillators $\{b_i\}$ through interactions of the form $\hat{a}^\dagger\hat{b}_i$ [8]. Encoding information into HOs has applications in quantum simulation [9–12], quantum communication [13–16], and continuous-variable quantum information processing [5, 17–21]. Conceptually, more quantum information can be stored in the high-dimensional Hilbert space of HOs, a potential advantage over qubits, if operations with sufficient fidelity and quantum error correction (QEC) [22] can be implemented. Crucially, information encoded in the HO needs to be preserved during processing and error correction.

Harmonic oscillators have been coupled directly in a number of systems [23–39], in some cases in the single-quantum regime and with full control of the HO states [40, 41]. However, these latter systems exhibited substantial decoherence rates relative to the achieved coupling rates. HOs have also been indirectly coupled by interacting with shared qubits [42–48].

In this work, we demonstrate direct coherent coupling of two HOs in the single-quantum regime with full state control and, crucially, coherence times much longer than the duration of a single state exchange. In general, the bilinear coupling of two HOs can be described by the Hamiltonian

$$H = \hbar g \left(e^{i\phi}\hat{a}\hat{b}^\dagger + e^{-i\phi}\hat{b}\hat{a}^\dagger \right), \tag{1}$$

where $2\pi\hbar$ is Planck's constant, $\hbar g$ is the coupling energy, and ϕ is a controllable phase. This coupling can lead to partial or full exchange of quantum states, as illustrated in Fig. 1a. Ideally, the timing, strength g, and phase ϕ of the coupling can be well controlled. To be practically useful, the coupling rates need to be much larger than decoherence rates of the coupled HO quantum states.

A linear string of N ions confined in a three-dimensional harmonic potential and subject to mutual Coulomb repulsion exhibits $3N$ normal modes of collective ion motion that can be treated as uncoupled HOs [49] (see Supplementary Material). These motional modes typically have coherence times of several milliseconds and can be manipulated by external electric fields [50], and by coupling to internal states of the ions using laser [51, 52] or microwave fields [51, 53–55]. In this way, individual modes can be initialized in a variety of quantum states [56] and information about the motion can be transferred to the internal states of ions, which are in turn read out by state-dependent fluorescence [57]. The recoil from photons scattered during readout typically

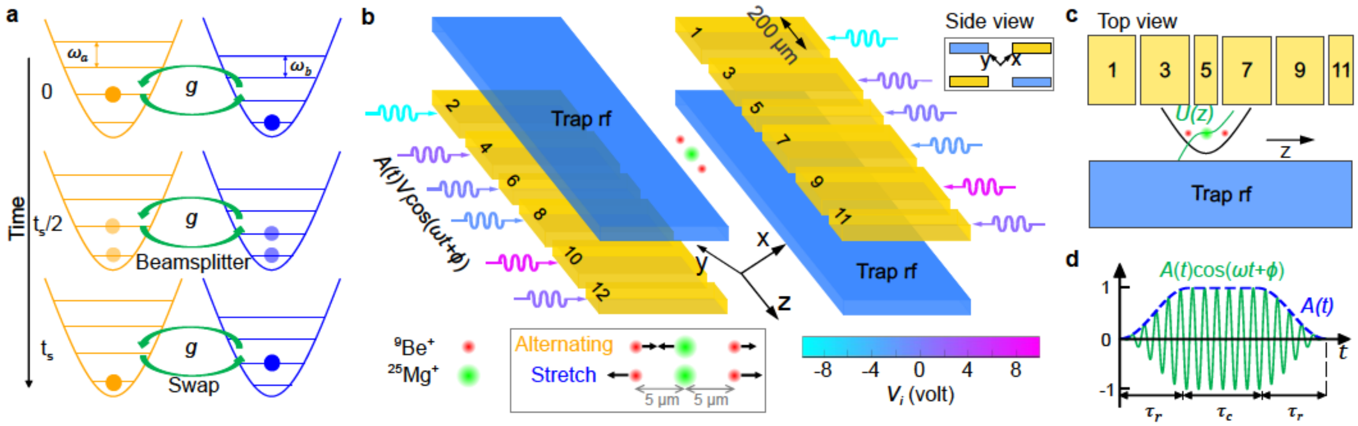

FIG. 1. **Coupled quantum mechanical oscillators.** **a**, Illustration of quantum state transfer between two coupled HOs. A coherent coupling (green) fully exchanges the states of two HOs up to a phase at t_s and creates two-mode entanglement at $t_s/2$, constituting a beamsplitter operation (see Supplementary Material). **b**, Three-dimensional perspective and **c**, top view of the trapping zone in a segmented Paul trap (not to scale). A ^{9}Be$^+$-^{25}Mg$^+$-^{9}Be$^+$ crystal is confined along the axial direction z in a harmonic potential well (solid black line in the top view). Two of three axial normal modes, "Alternating" at 3.66 MHz and "Stretch" at 3.38 MHz (mode participation vectors ξ for all ions visualized as arrows in the dashed box at the bottom), are coupled by an oscillating electric potential $U(z,t) = U(z)A(t)\cos(\omega t+\phi)$. The coordinate origin is at the location of the Mg$^+$ ion, and the spatial dependence of $U(z) = U_0 z^3$ is visualized by the green curve in **c**. The potential is generated from twelve synchronized rf drives $V_i A(t)\cos(\omega t+\phi)$ ($i = 1, ..., 12$, with V_i represented by the color of wavy arrows) applied to twelve control electrodes (gold). **d**, Coupling pulse shape in the experiments. Green oscillating line represents the temporal dependence of $U(z,t)$ under the amplitude envelope $A(t)$ (blue dashed line).

perturbs the ion motion and destroys its quantum coherence. Here, we couple pairs of normal modes by applying an electric potential with suitable spatial dependence that oscillates at the difference of two mode frequencies, and investigate the properties of such coupling operations. In particular, we can couple to a mode of motion whose symmetry protects it from perturbations during readout. This enables us to perform minimally disturbing measurements of the mode, projecting its state but not otherwise affecting it. To demonstrate this essential element of continuous-variable QEC, we repeatedly test whether the protected mode is in its ground state while preserving the state to a high degree.

We consider two normal modes a and b at frequencies ω_a and ω_b, with position coordinates $\delta r_{n,i_a}$ and $\delta r_{n,i_b}$ referring to the displacement relative to equilibrium of the nth ion along direction i_a or i_b, where $i_a, i_b \in \{x, y, z\}$. To couple these modes, we apply an oscillating and spatially-varying electric potential

$$U(\boldsymbol{r},t) = U(\boldsymbol{r})A(t)\cos(\omega t+\phi), \tag{2}$$

with $0 \leq A(t) \leq 1$ a pulse envelope (blue dashed line in Fig. 1d) that evolves slowly compared to $2\pi/\omega$, and $\omega \approx |\omega_a - \omega_b|$. The modes are coupled by curvature terms

$$\alpha_n = \frac{\partial^2 U}{\partial i_a \partial i_b}\Big|_{\boldsymbol{r}=\boldsymbol{r}_{n,0}} \tag{3}$$

in the expansion of $U(\boldsymbol{r})$ around the equilibrium position $\boldsymbol{r}_{n,0}$ of the nth ion. After transforming to the interaction picture and neglecting fast-rotating terms (see Supplementary Material), the interaction Hamiltonian has the form of Eq.(1) with $g(t) = A(t)g_0$. The coupling strength g_0 is a sum over contribution from each ion

$$g_0 = \sum_{n=1}^{N} g_n = \sum_{n=1}^{N} \frac{Q_n \alpha_n}{4M_n\sqrt{\omega_a\omega_b}} \xi_{n,a}^{(i_a)} \xi_{n,b}^{(i_b)}, \tag{4}$$

where Q_n, M_n, $\xi_{n,a}^{(i_a)}$ and $\xi_{n,b}^{(i_b)}$ denote the charge, mass and participation in modes a and b of the nth ion. The participation is defined as the nth ion's component of the normalized eigenvector of a given normal mode. A particular contribution g_n can be positive or negative and g_0 can be influenced by properly designing the curvatures α_n to constructively add when multiplied with the mode participations. For example, when two identical ions are subject to the same curvature $\alpha_1 = \frac{\partial^2 U}{\partial x \partial z}|_{\boldsymbol{r}=\boldsymbol{r}_{1,0}} = \alpha_2$, the coupling between modes a and b, where the two ions oscillate in phase along the z axis and out of phase along the x axis respectively, will vanish, because $\xi_{1,a}^{(z)}\xi_{1,b}^{(x)} = -\xi_{2,a}^{(z)}\xi_{2,b}^{(x)}$. If instead the oscillating potential fulfills $\alpha_1 = -\alpha_2$, the coupling terms add constructively.

Atomic motion is extremely fragile and can be significantly perturbed by a single photon recoil. However, if photon recoil can be limited to a certain ion s that does not participate in a mode a, *i.e.* $\xi_{s,a}^{(i_a)} = 0$, this mode is protected and largely unperturbed even if thousands of photons are scattered from ion s. The coupling Eq.(1) enables "swapping" of the state in mode a into a suitable mode b where $\xi_{s,b}^{(i_b)} \neq 0$ and subsequently, information

$\mathcal{S}$

$\mathcal{S}$

$\mathcal{N}$

$\mathcal{N}$

$\mathcal{S}$

$\mathcal{N}$

$\mathcal{N}$

$\mathcal{N}$

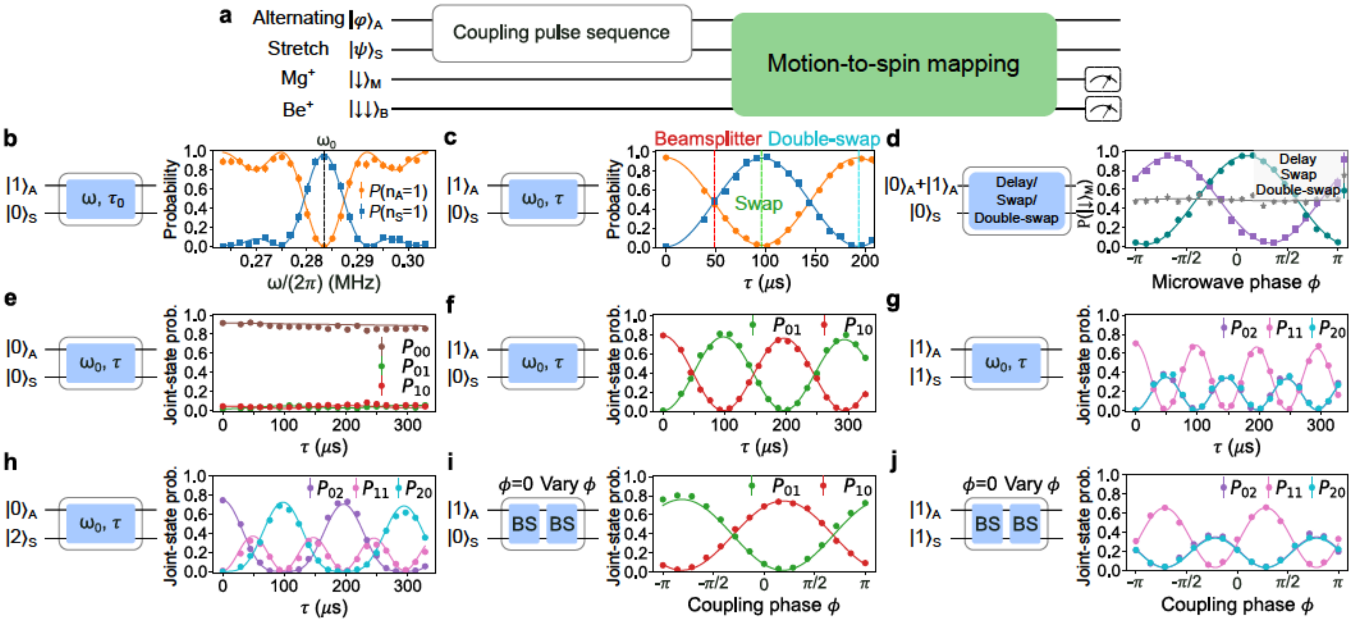

FIG. 2. **Coherent coupling dynamics.** **a**, Experimental sequence for characterizing Alternating-Stretch coupling. The modes are cooled to near the ground state, then prepared in a certain state by Raman laser interactions. A coupling pulse sequence (white box) coherently exchanges the states between modes. Motional states are mapped onto one or both of the ion species by Raman laser interactions (green box, see details in text) followed by state-dependent fluorescence detection. The respective initial motional states and coupling pulse sequences (blue boxes represent single coupling pulses) are indicated in **b-j**. Lines in **b-d** are fits to the data, while lines in **e-j** are from numerical simulation using experimentally calibrated parameter values. **b**, When a single phonon is prepared in the Alternating mode, the probability of finding the phonon in the Alternating mode is high unless the coupling frequency ω is tuned near resonance, where the probability then becomes high for the phonon to be exchanged into the Stretch mode (blue squares). **c**, With the coupling held on resonance, a single phonon coherently swaps between the two modes as the coupling time τ increases. Vertical dashed lines in different colors indicate the pulse durations for beamsplitter (BS), swap, and double-swap operations respectively. **d**, Motional coherence verification after a coupling pulse. A superposition of $|0\rangle_A$ and $|1\rangle_A$ undergoes a swap operation (grey stars), a double-swap operation (teal dots), or a delay (purple squares) equivalent to the duration of the double-swap operation. Then, the motional superposition is mapped onto Mg$^+$ hyperfine states $|\uparrow\rangle_M$ and $|\downarrow\rangle_M$ with a variable phase ϕ. **e-h**, Probability of finding certain states in $\mathcal{S}$ as the exchange duration τ is swept for four different initial states. **i**,**j**, Phonon interference for initial states $|1\rangle_A\,|0\rangle_S$ and $|1\rangle_A\,|1\rangle_S$. Results in (**f**, **i**) and (**g**, **j**) verify two-mode entanglement generated by a beamsplitter for initial states $|1\rangle_A\,|0\rangle_S$ and $|1\rangle_A\,|1\rangle_S$ respectively. Results in (**g**, **j**) correspond to Hong-Ou-Mandel-type interference between two phonons at different frequencies.

Mg$^+$ fluorescence detection. Due to the limited collection and detection efficiency of our apparatus, we detect approximately 30 photons on average when in the bright state, while the total number of photons scattered into all directions is several thousand. In each measurement, we declare the Mg$^+$ ion to be bright or dark depending on whether or not the number of detected photons is greater than nine. The in-phase (INPH) mode and the Alternating mode are cooled to near their ground states and another swap pulse transfers the number state back to the Alternating mode to permit the next measurement. This particular measurement cannot distinguish number states with $n > 1$, but can be adapted in principle to reveal any single bit of information about the state of the motion by simply modifying the mapping sequence, which may make it amenable to syndrome extraction in bosonic error correction codes [17, 19, 63, 64].

As a demonstration, the Alternating mode is sideband cooled to a thermal distribution with an average occupation of $\bar{n} = 0.023(1)$, with more than 99.9% of the population in $|0\rangle$ (p_0=0.978(1)) and $|1\rangle$ (p_1=0.022(1)). We repeat the motional state measurement up to three times and obtain a series of outcomes $\{o_1, ..., o_i, ..., o_N\}$ with $o_i \in \{d, b\}$, i=1,..., N. For M1, we declare the state is $|0\rangle$ or $|1\rangle$ if all N outcomes are the same (all d or all b, respectively), and discard the other outcomes because the state is not distinguished faithfully. The relative frequencies of finding $|0\rangle$ and $|1\rangle$, defined as $\tilde{p}_0 = p(\{d\}_N)/(p(\{d\}_N) + p(\{b\}_N)$ and $\tilde{p}_1 = 1 - \tilde{p}_0$, should match with the initial distribution $\{p_0, p_1\}$, where $p(\{d\}_N)$ and $p(\{b\}_N)$ are the probabilities of all N outcomes being d and b respectively. For M2, the roles of d and b are exchanged. We examine the final state of the Alternating mode by applying a π pulse on the motion-adding-sideband (MAS) transition $|\downarrow\rangle_M\,|0\rangle \leftrightarrow |\uparrow\rangle_M\,|1\rangle$ or a pulse of the same duration on the MSS transition, followed by Mg$^+$ fluorescence detection. The $\bar{n}$ conditioned on various measurement outcomes can be estimated with

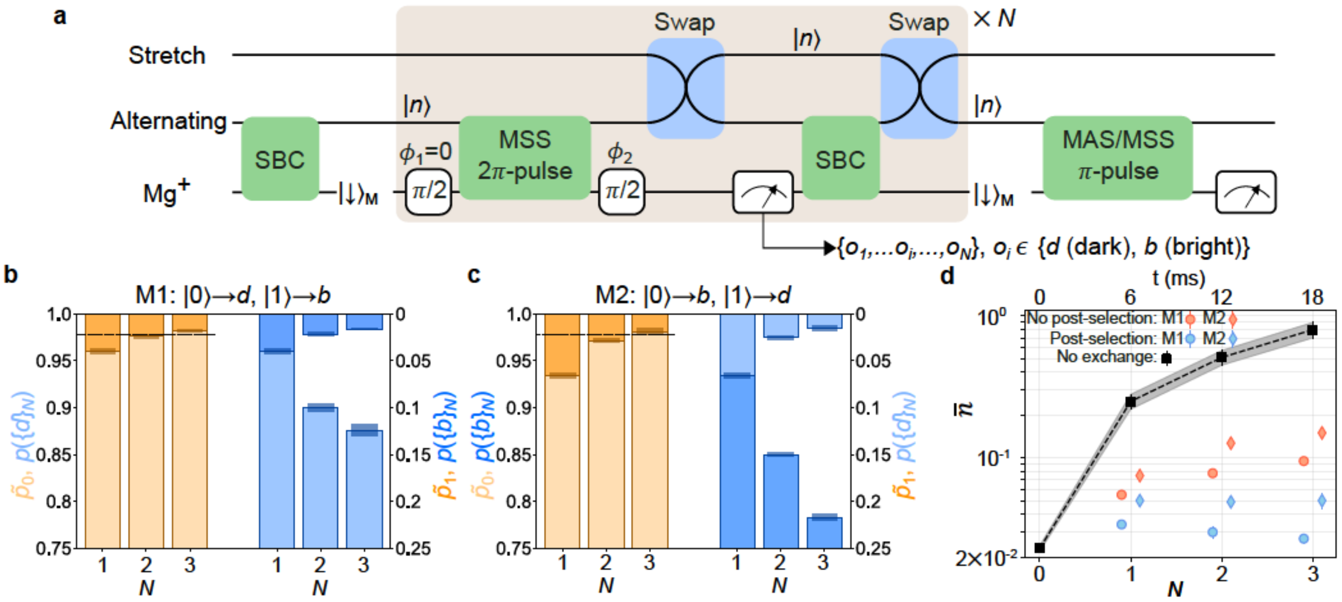

FIG. 3. **Repeated measurements of quantum ground state of trapped-ion motion.** **a**, Diagram of measurement for non-destructively distinguishing number states $\{|0\rangle, |1\rangle\}$. The Alternating mode is initialized in a thermal distribution at $\bar{n} = 0.023(1)$, with > 0.999 of the population in $|0\rangle$ (p_0=0.978(1)) and $|1\rangle$ (p_1=0.022(1)). These states can be distinguished with the operations in the grey box (see text) and read out on Mg^+ after swapping the motional state into the Stretch mode to protect it from the recoil of the Mg^+ ion during detection and sideband cooling (SBC). Another swap pulse brings the motional state back to the Alternating mode such that this measurement can be repeated. In each repetition, Mg^+ is declared either bright (b) or dark (d) by comparing the detected photon number with a threshold of nine. We obtain a series of binary outcomes $\{o_1, ..., o_i, ..., o_N\}$, $o_i \in \{d, b\}$ with the measurement performed N times. When $\phi_2 = 0$, we realize the mapping (M1): $|0\rangle \to d$, $|1\rangle \to b$, while $\phi_2 = \pi$ exchanges the roles of b and d, (M2): $|1\rangle \to d$, $|0\rangle \to b$. We verify the motional state after a certain sequence by measuring MAS and MSS excitation. **b** and **c**, Repeated measurement outcomes match the initial distribution. For M1 (**b**), we declare the state is $|0\rangle$ ($|1\rangle$) if all N outcomes are d (b), which occurs with probability $p(\{d\}_N)$ ($p(\{b\}_N)$). The relative frequencies of finding $|0\rangle$ and $|1\rangle$, $\{\tilde{p}_0$ (light orange bars), $\tilde{p}_1$ (dark orange bars)$\}$ extracted (see text) from $p(\{d\}_N)$ (light blue bars) and $p(\{b\}_N)$ (dark blue bars), are consistent with $\{p_0, p_1\}$ (dashed line). As N increases, $\{\tilde{p}_0, \tilde{p}_1\}$ become closer to the initial distribution but use less data, *i.e.* the sum of $p(\{d\}_N)$ and $p(\{b\}_N)$ decreases. For M2 (**c**), we identify the state as $|0\rangle$ or $|1\rangle$ if all N outcomes are b or d and observe similar results. **d**, Alternating mean occupation number ($\bar{n}$) post-selected on all N outcomes being d for M1 (blue dots) or b for M2 (blue diamonds) are lower than the corresponding $\bar{n}$ with no post-selection (red symbols). "No exchange" $\bar{n}$ (black squares), which are measured after applying a delay with the duration of N measurement blocks without swapping into the Stretch mode, are substantially higher than other results due to the higher heating rate of the Alternating mode. Data points are laterally offset from nominal N values for legibility and error bars for some points are smaller than the plot symbols.

MAS and MSS transition probabilities, if the conditioned state is close to a thermal state, or if the population is predominantly in $|0\rangle$ and $|1\rangle$ [52].

In Fig. 3b, using M1 and N=1, we detect $\{d\}$ heralding $|0\rangle$ and obtain $\tilde{p}_0$ (light orange bar)=$p(\{d\})_{N=1}$ (light blue bar)=0.960(3) while $\tilde{p}_1$ (dark orange bar)=$p(\{b\})_{N=1}$ (dark blue bar)$\,=\,$0.040(3). The $\{\tilde{p}_0$, $\tilde{p}_1\}$ are close to the initial state populations $\{p_0, p_1\}$ (indicated by dashed line) respectively with a small difference of about 0.02, which indicates a detection error. With $N = 2$, the $\{\tilde{p}_0$, $\tilde{p}_1\}$ are only different from $\{p_0$, $p_1\}$ by 0.002(2) because the state is heralded twice, largely suppressing erroneous declarations. However, we discard about 7.8% of the total trials (gap between light blue and dark blue bars) where the outcomes from the two rounds disagree. This number is larger than the detection error of a single round, indicating that the motional state is slightly changed during the measurements, likely due to heating. With $N = 3$, the $\{\tilde{p}_0, \tilde{p}_1\}$ are also close to the initial distribution, but another 3% of the total trials are discarded. In Fig. 3c, we implemented M2 and observed that $\{\tilde{p}_0, \tilde{p}_1\}$ also match well with the initial distribution. Compared to M1, more data were discarded due to disagreement between repeated measurements, suggesting that Mg^+ scattering may introduce additional disturbance to the motional state. For larger N with either M1 or M2, the leakage into higher number states also increases because of heating and may lower the readout fidelity.

The $\bar{n}$ values of final motional states as determined by MAS/MSS transition rates are shown in Fig. 3d. The black data points represent $\bar{n}$ after waiting an equiva-

We observe significant off-resonant excitation of the axial in-phase mode (at $\sim 1.5\,\text{MHz}$) of a BMB crystal when using a square coupling pulse around the resonant frequency of the Alternating-Stretch coupling, while such excitation is largely suppressed with shaped pulses.

We determine the coupling drive amplitudes for the twelve electrodes using a trap potential simulation [58] to generate a potential for which the desired spatial derivative is maximized while the unwanted components are minimized. These unwanted terms typically include the gradients $\partial U/\partial i$, $i \in \{x, y, z\}$, which displace and potentially heat the ion motion, and the curvatures $\partial^2 U/\partial i^2$, $i \in \{x, y, z\}$ which modulate motional frequencies. Higher-order derivatives of the potential are typically negligible in our trap and are not considered in the simulations.

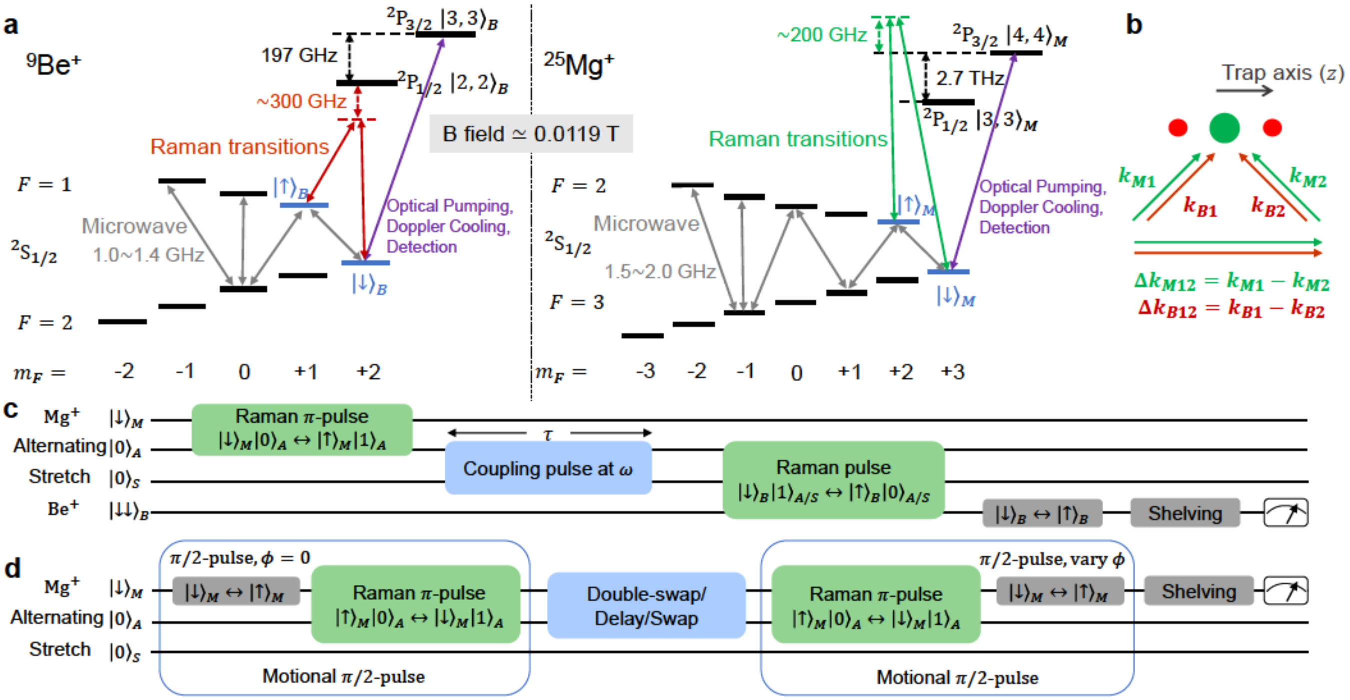

FIG. 4. **a**, Relevant electronic states of $^9\text{Be}^+$ and $^{25}\text{Mg}^+$ at an applied magnetic quantization field of $|\vec{B}| \approx 0.0119$ T. **b**, Configuration of Raman laser beams for Be^+ (red) and Mg^+ (green). **c**, Experimental sequence for calibrating coupling resonant frequency and rates (results in Fig. 2**b**,**c**) of the Alternating-Stretch coupling. **d**, Experimental sequence for a motional Ramsey interference experiment between $|0\rangle_A$ and $|1\rangle_A$ (results in Fig. 2**d**) with a delay, or a coupling pulse for a single swap or a double swap inserted between the motional $\pi/2$ pulses.

Ion species and state manipulation

We trap two ion species, $^9\text{Be}^+$ and $^{25}\text{Mg}^+$, at a quantization magnetic field of $\sim 0.0119\,\text{T}$. The relevant electronic states of both species are illustrated in Fig. 4a. A σ^+-polarized ultraviolet (UV) laser beam near 313 nm optically pumps Be^+ ions to $|{\downarrow}\rangle_B = {}^2S_{1/2}\,|F = 2, m_F = 2\rangle_B$, while Doppler cooling and state-dependent fluorescence detection are implemented with a second UV laser beam driving the ${}^2S_{1/2}\,|2, 2\rangle_B \leftrightarrow {}^2P_{3/2}\,|3, 3\rangle_B$ cycling transition, causing photons to be emitted from the ion when Be^+ is in the “bright” state $|{\downarrow}\rangle_B$. Similarly, Mg^+ ions are optically pumped to the bright state $|{\downarrow}\rangle_M = {}^2S_{1/2}\,|3, 3\rangle_M$ with a σ^+-polarized laser beam near 280 nm. A second UV laser beam is used to drive the ${}^2S_{1/2}\,|3, 3\rangle_M \leftrightarrow {}^2P_{3/2}\,|4, 4\rangle_M$ transition for Doppler cooling and fluorescence detection.

State-dependent fluorescence detection is accomplished with resonant UV light illuminating the ions for a duration of $330\,\mu\text{s}$ for Be^+ and $200\,\mu\text{s}$ for Mg^+, with a fraction of the ion fluorescence collected by an achromatic imaging system and detected by a photomultiplier tube. To distinguish two hyperfine states of interest, we apply a “shelving” sequence that consists of microwave π pulses to transfer one hyperfine state to the bright state and the other to a dark state (a hyperfine state away from the bright state in the ${}^2S_{1/2}$ manifold) before fluorescence detection. The microwave transitions used in the shelving sequence are indicated with grey double-arrows in

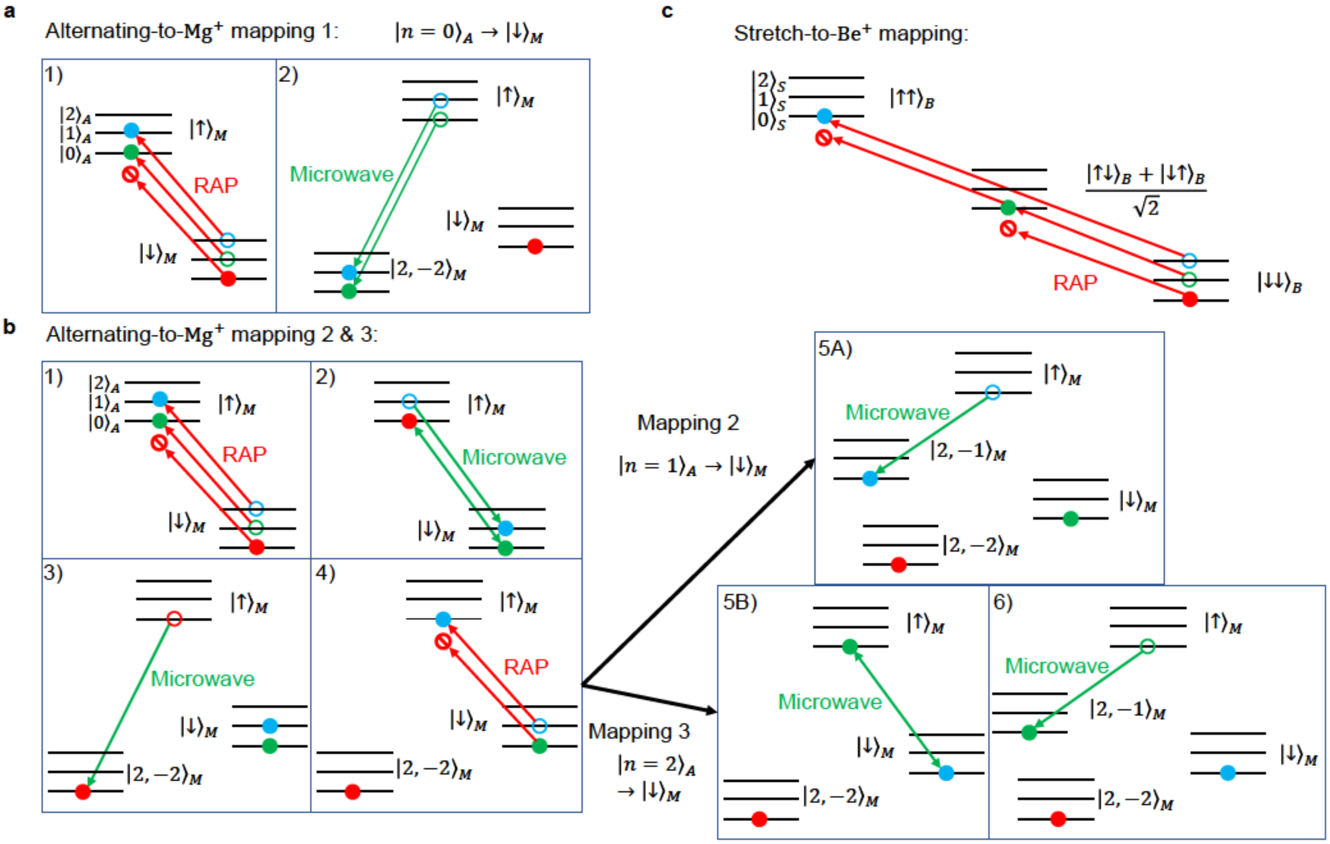

FIG. 5. Diagram of motion-to-spin mapping for determining joint populations of motional modes. Circles in different colors represent the initial population in $|n=0\rangle$ (red), $|1\rangle$ (green), $|2\rangle$ (blue) at the beginning of the illustrated step and solid dots at the end. Transitions are indicated by arrows and forbidden transitions are indicated by a prohibitory symbol at the tip of the arrow.

- $|1\rangle_A |0\rangle_S$ is prepared from $|0\rangle_A |0\rangle_S$ with a microwave π pulse on the $|\downarrow\rangle_M \rightarrow |\uparrow\rangle_M$ transition, followed by a sideband π pulse on $|\uparrow\rangle_M |0\rangle_A \rightarrow |\downarrow\rangle_M |1\rangle_A$, which injects a single phonon into the Alternating mode and leaves Mg$^+$ in $|\downarrow\rangle_M$. The microwave pulse has negligible error and the sideband π pulse has an error of about 0.03, in large part due to the Debye-Waller effect from the axial in-phase mode [51]. When such an error occurs, the sideband π pulse is incomplete and leaves the Mg$^+$ ion partially in $|\uparrow\rangle_M$. Therefore, we apply an additional dissipative laser repumping pulse to ensure the Mg$^+$ ion is reset to $|\downarrow\rangle_M$ before joint state mapping.
- $|1\rangle_A |1\rangle_S$ is prepared by initializing in $|1\rangle_A |0\rangle_S$, as described above. Then, a calibrated swap pulse transfers (with an infidelity of approximately 0.01) the single phonon from the Alternating mode to the Stretch mode ($|0\rangle_A |1\rangle_S$). Then, another single phonon is injected into the Alternating mode using the same method described above, resulting in $|1\rangle_A |1\rangle_S |\downarrow\rangle_M$.
- $|0\rangle_A |2\rangle_S$ is prepared from $|0\rangle_A |0\rangle_S$ by injecting two phonons into the Stretch mode by globally addressing two Be$^+$ ions with a microwave carrier π pulse on $|\downarrow\rangle_B \rightarrow |\uparrow\rangle_B$, followed by a sideband RAP pulse (with an error of approximately 0.05) on the transition $|\uparrow\rangle_B |n\rangle_S \rightarrow |\downarrow\rangle_B |n+1\rangle_S$. Afterwards, a Be$^+$ repumping pulse is applied to reset the internal states to $|\downarrow\downarrow\rangle_B$ in case the RAP pulse did not leave the ions in that state.

For motional state analysis, we map the population of joint-number states in the subspace $\mathcal{S} = \{|0\rangle_A, |1\rangle_A, |2\rangle_A\} \bigotimes \{|0\rangle_S, |1\rangle_S, |2\rangle_S\}$ onto the internal states of two ion species. Two steps, Alternating-to-Mg$^+$ mapping and Stretch-to-Be$^+$ mapping, are sequentially implemented. The mapping is described in detail in the following and illustrated in Fig. 5.

- Alternating-to-Mg$^+$ mapping: One of three different mapping sequences (Fig. 5a, b) maps the population in one of the three lowest number states respectively onto the bright state $|\downarrow\rangle_M$ and shelves the other two number states to dark states, $|2,-1\rangle_M$ and $|2,-2\rangle_M$. Repeated experimental trials with different choices of mapping

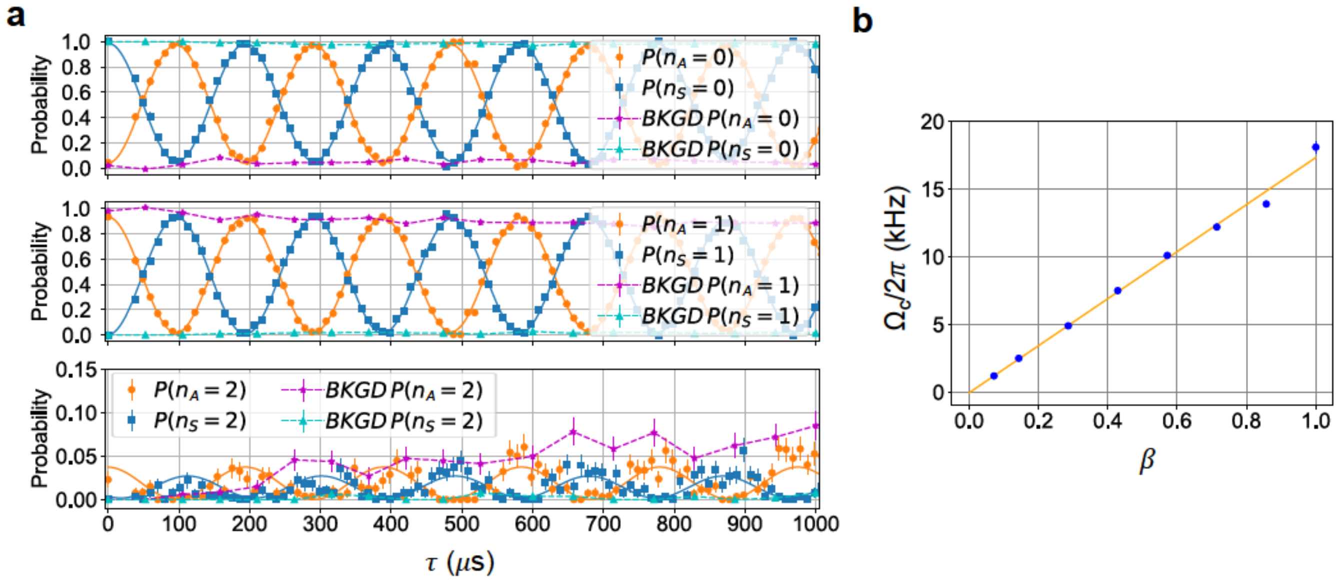

FIG. 6. **Characterization of the Alternating-Stretch coupling.** **a**, With the Alternating and Stretch mode prepared in $|1\rangle_A |0\rangle_S$, the probabilities of the Alternating (orange dots) and Stretch (blue squares) modes in number state n=0 (top), n=1 (middle, also partially shown in Fig. 2c), n=2 (bottom), oscillate as the coupling pulse duration is varied while the coupling frequency is held on resonance. As references, we repeat the experiment by replacing the coupling pulse with a delay of the same duration to investigate effects of heating, and show the corresponding probabilities of certain number states in the Alternating (magenta stars) and Stretch (cyan triangles) modes in the three panels. The population mostly stays in n=0 and n=1, while oscillating out of phase between the two modes at $\Omega_c = 2g_0$. In the bottom panel, the populations in n=2 of the two modes show small oscillations (due to imperfect state preparation) on top of a slowly growing background that is roughly the average heating rate of the two coupled modes, as independently verified by the reference data (magenta stars and cyan triangles). Solid lines are fits to the data and dashed lines are the guides to the eye. **b**, The population exchange rate Ω_c can be varied by controlling the amplitude of the coupling potential with a relative factor $0 \leq \beta \leq 1$, such that $U(\mathbf{r}) = \beta U_{max}(\mathbf{r})$. This is accomplished by scaling the oscillating potential amplitude of electrode i with $V_i = \beta V_{max,i}$ for all twelve electrodes ($i = 1, 2, ..., 12$). We choose β=0.286 for all other results presented in this work. Using higher β causes larger unintended excitation of the INPH mode.

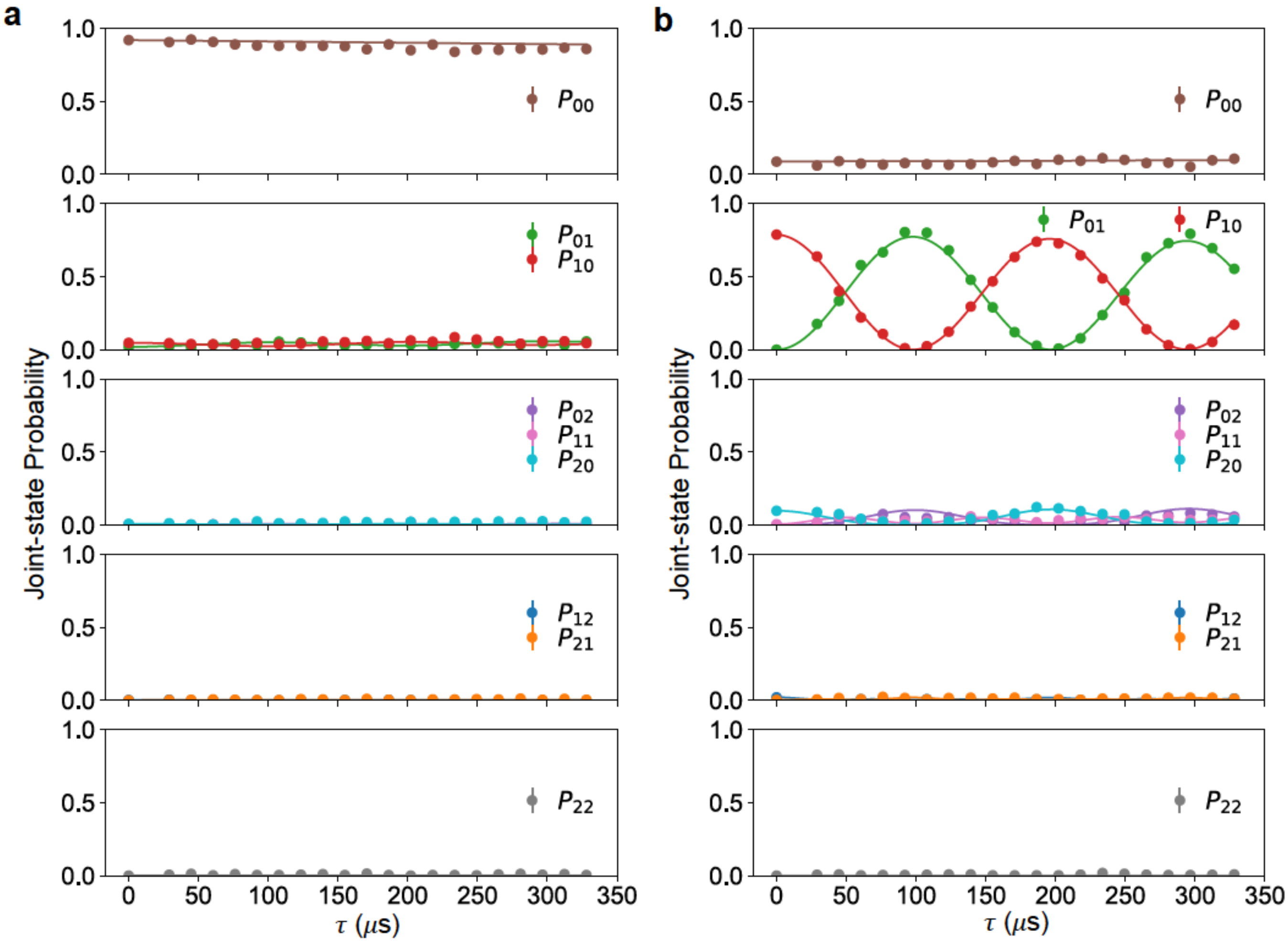

FIG. 7. **Joint-motional population dynamics: Coupling time scans I.** The two normal modes are prepared in (a) $|0\rangle_A |0\rangle_S$ or (b) $|1\rangle_A |0\rangle_S$. The plots show population in the nine joint number states of the Alternating mode and the Stretch mode as a function of coupling time τ in five separate panels with (from top to bottom) 0 to 4 total quanta of motion in the two modes. Imperfect state preparation and measurement cause the population of the target initial state to deviate from one at $\tau = 0$ while the other state populations may start with a non-zero value. More detailed descriptions of the experiments can be found in the main text.

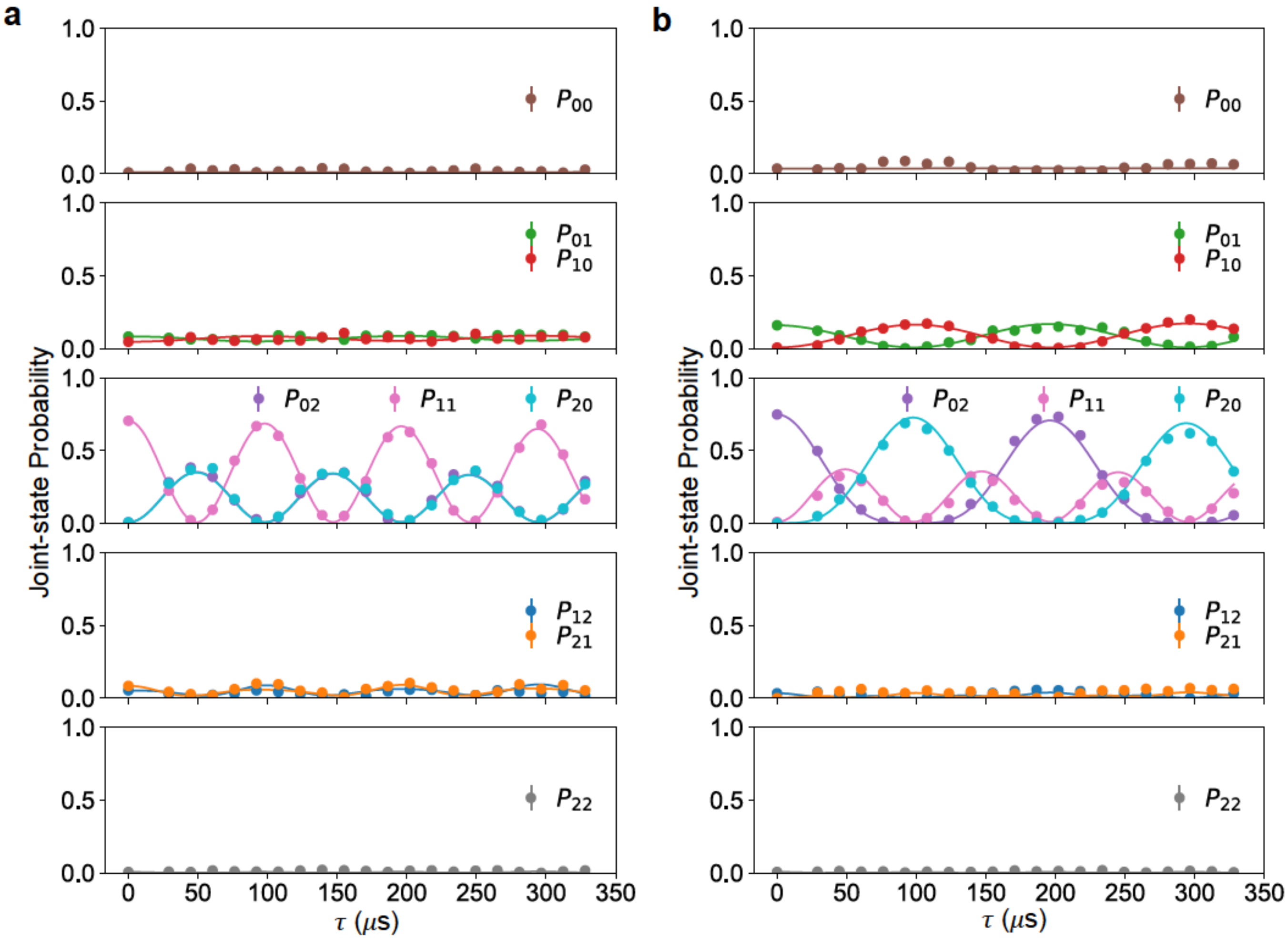

FIG. 8. **Joint-motional population dynamics: Coupling time scans II.** The Alternating and Stretch modes are prepared in (a) $|1\rangle_A\,|1\rangle_S$, (b) $|0\rangle_A\,|2\rangle_S$.

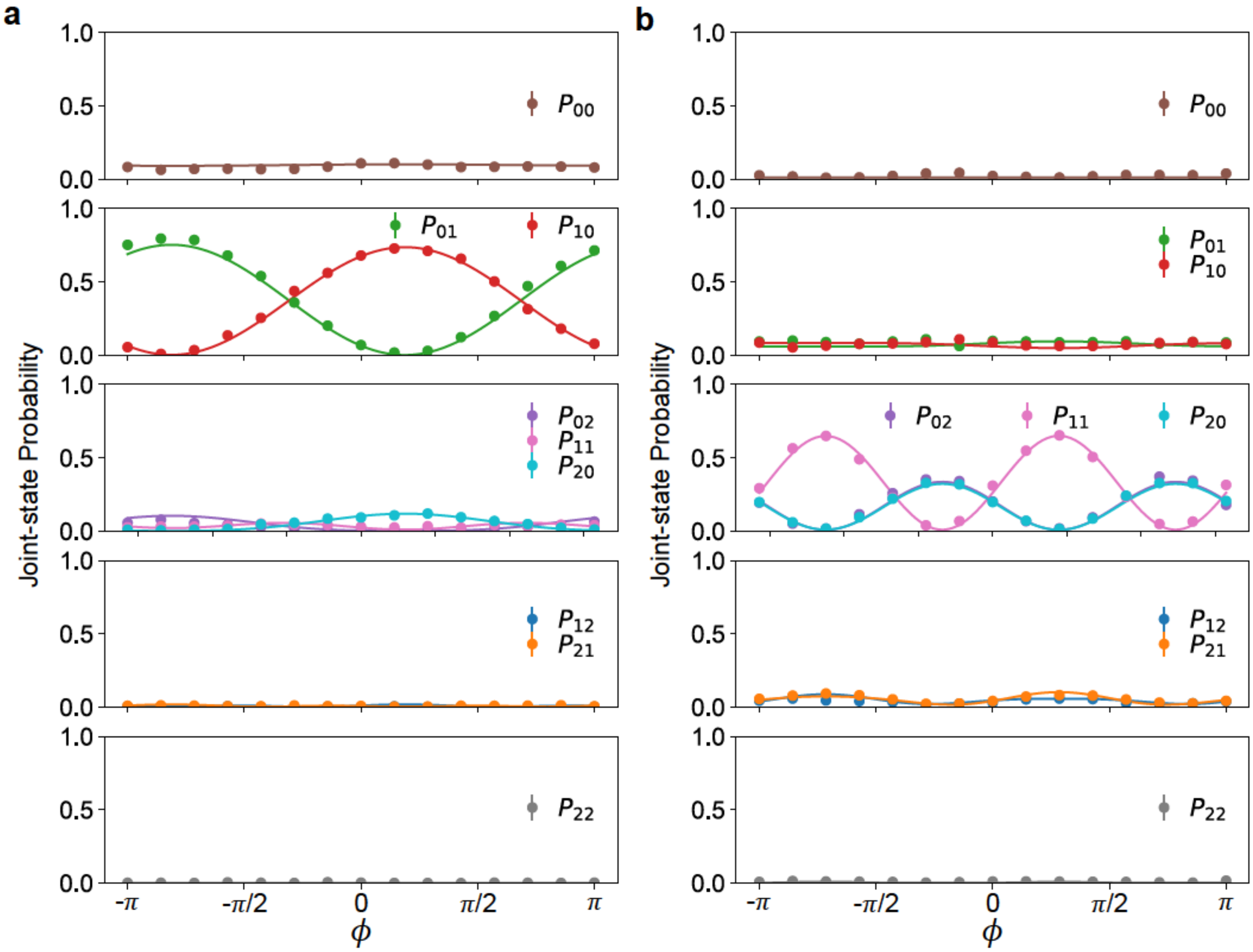

FIG. 9. **Joint-motional population dynamics: Coupling phase scans.** Phonon interference with the initial states (a) $|1\rangle_A |0\rangle_S$ and (b) $|1\rangle_A |1\rangle_S$. The results in the second panel of **a** and the third panel of **b** are also shown in Fig. 2**i** and **j** of the main text.

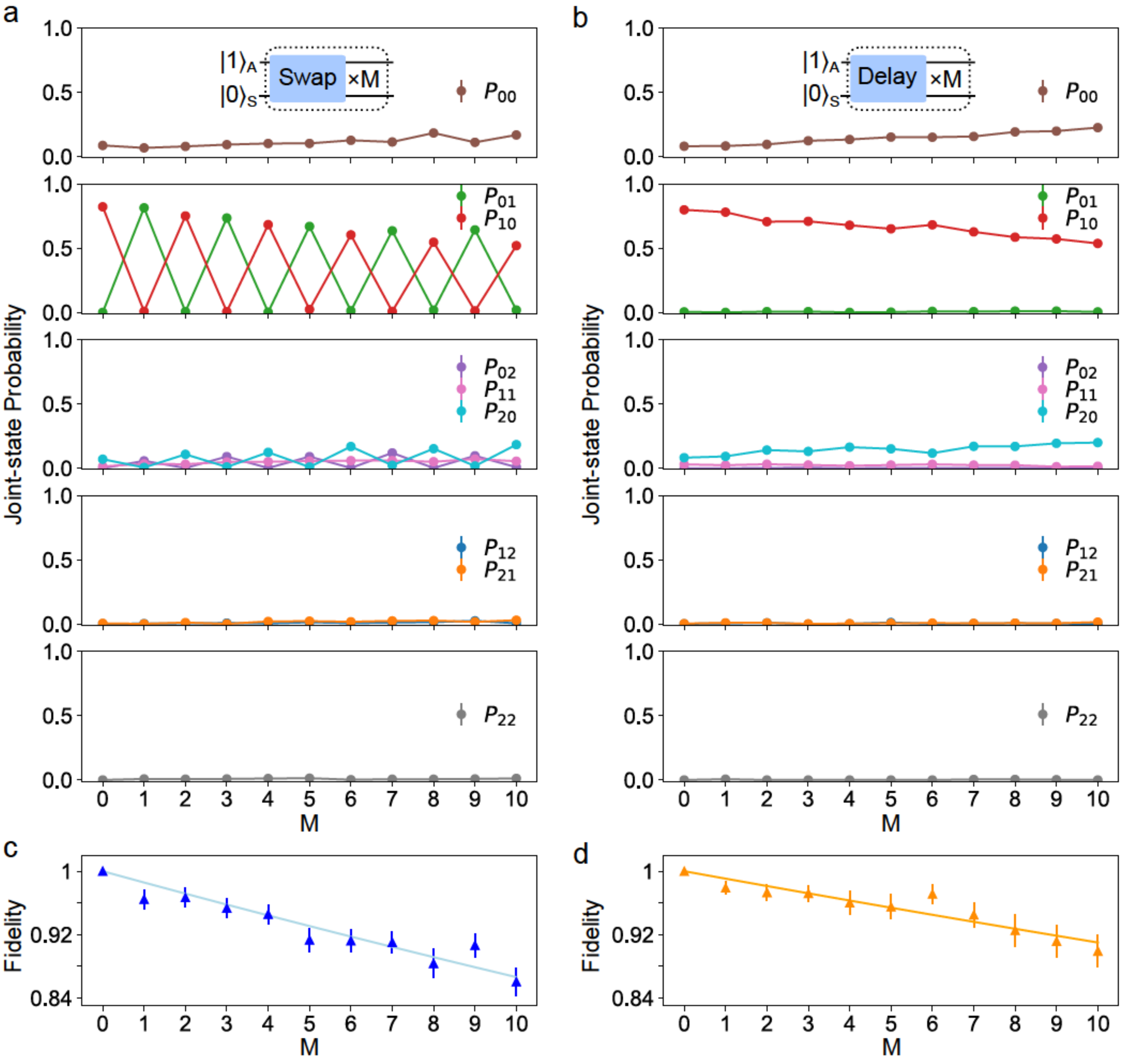

FIG. 10. **Joint-motional population dynamics during repeated swap operations.** **a**, With the two modes prepared in $|1\rangle_A |0\rangle_S$, we apply M swap pulses and measure the populations of the two-mode joint states. The second panel shows that the injected single phonon is swapped between the two modes. The sum of populations in the second panel decreases as the number M of swap operations increases, while the populations of the states shown in the first and third panel grow because of heating. **b**, Data from a reference experiment where the coupling pulses are replaced with delays of equal duration to illustrate the effect of heating. In this case, no population is exchanged and only a slow population leakage from the initial state (red dots in the second panel) to primarily $|0\rangle_A |0\rangle_S$ (dots in the first panel) and $|2\rangle_A |0\rangle_S$ (blue dots in the third panel) is observed. This is due to a much larger heating rate in the Alternating mode compared to the Stretch mode. Solid lines in **a** and **b** serve as guides to the eye. **c**, With the population of all nine joint states, we estimate the fidelity of the final density matrix σ compared to the target density matrix ρ where ideal swaps are applied to an initial density matrix (data at $\mathrm{M}=0$ in **a**). We treat the density matrices σ and ρ as a fully decohered mixture of nine joint number states (only diagonal terms are non-zero) and estimate the fidelity with $F = (Tr\sqrt{\sqrt{\rho}\sigma\sqrt{\rho}})^2$. We fit the fidelities (blue triangles) to $F(\mathrm{M}) = (1-\epsilon)^{\mathrm{M}}$ to extract an error ϵ per swap operation to be 1.4(1)%. **d**, The same analysis is performed for the reference experiment data (orange triangles) where the fidelity to the initial density matrix (data at $\mathrm{M}=0$ in **b**) is shown and fitted, yielding an error per swap time of 0.9(1)%. The error of the swap operation is dominated by heating, which can be suppressed by increasing the coupling strength to reduce the swap time, or by lowering the heating rate, for example by operating in a similar trap at cryogenic temperatures.

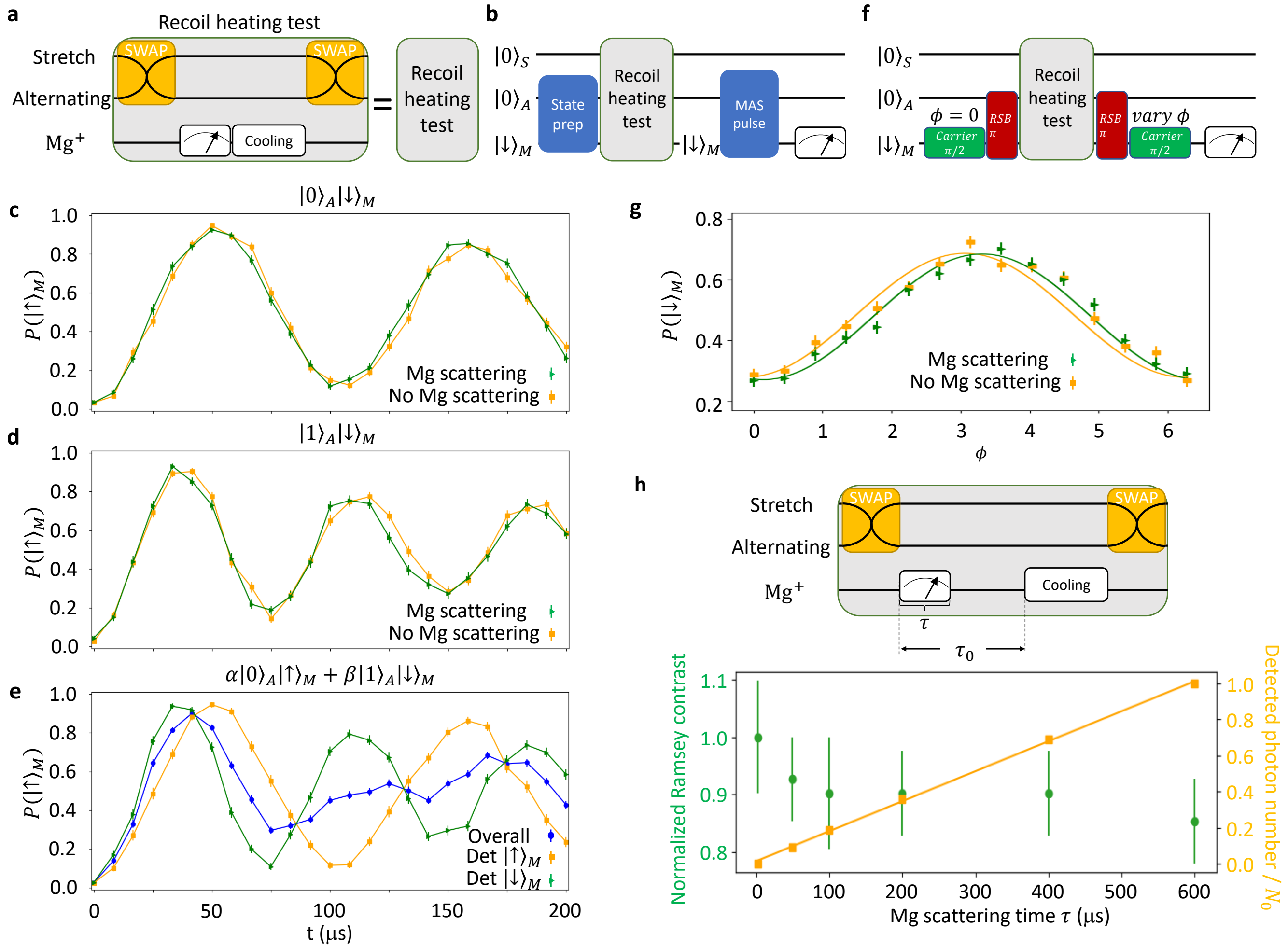

A M A M A M A M

M M

A A

A A A A

A A M M _

M A M A A A M

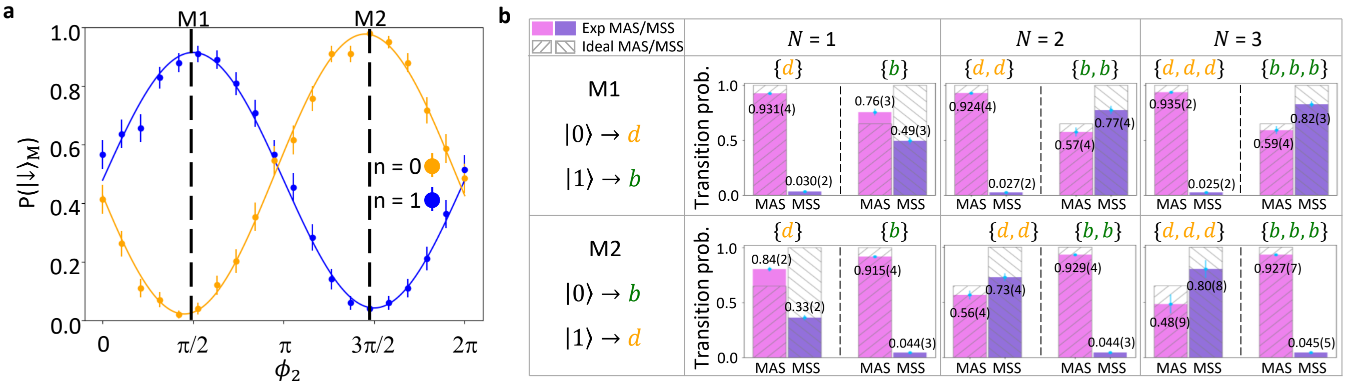
a
M1
M2
1.0
0.8
0.6
0.4
0.2
0.0
P(|↓⟩_M)
n = 0
n = 1
0
π/2
π
3π/2
2π
ϕ₂
b
Exp MAS/MSS
Ideal MAS/MSS
N = 1
N = 2
N = 3
M1
|0⟩ → d
|1⟩ → b
M2
|0⟩ → b
|1⟩ → d
{d}
{b}
{d, d}
{b, b}
{d, d, d}
{b, b, b}
Transition prob.
1.0
0.5
0.0
MAS MSS
0.931(4)
0.030(2)
0.76(3)
0.49(3)
0.924(4)
0.027(2)
0.57(4)
0.77(4)
0.935(2)
0.025(2)
0.59(4)
0.82(3)
0.84(2)
0.33(2)
0.915(4)
0.044(3)
0.56(4)
0.73(4)
0.929(4)
0.044(3)
0.48(9)
0.80(8)
0.927(7)
0.045(5)

A A